Wind and Structures, *Vol. 30, No. 6 (2020) 559-573*
DOI: https://doi.org/10.12989/was.2020.30.6.559

POD Analysis for modeling wind pressures and wind effects of a cylindrical shell roof

Fanghui Li[1] and Xinzhong Chen*[2]

[1]*College of Civil Engineering, Heilongjiang University, Harbin 150086, P.R. China*
[2]*National Wind institute, Department of Civil, Environmental, and Construction Engineering, Texas Tech University, Lubbock TX 79409, U.S.A.*

(*Received August 11, 2019, Revised March 3, 2020, Accepted April 29, 2020*)

Abstract. This paper presents a study on the effectiveness of the proper orthogonal decomposition (POD) technique for reconstruction of wind pressure field as applied to a cylindrical shell roof based on simultaneously measured wind pressure data. The influence of wind loading mode truncation on the statistics of dynamic pressures and wind load effects are investigated. The results showed that truncation of higher wind loading modes can have more noticeable influence on the maximum and minimum pressures that the standard derivation (STD) values. The truncation primarily affects the high-frequency content of the pressures. Estimation of background response using wind loading modes is more effective than the use of traditional structural modal analysis.

Keywords: proper orthogonal decomposition; wind tunnel test; wind-induced response; equivalent static wind load; low-rise roof

1. Introduction

Wind load on low-rise buildings are complicated by the variety of geometric configurations, wind characteristics, direction and terrain categories. The dynamic wind pressures on building surface measured in wind tunnel using synchronous pressure measurement system provide a detailed description of spatiotemporal characteristics of wind loading. The wind pressures on a wide range of curved roof models with different dimensions were investigated in wind tunnel (Franchini *et al*. 2005, Blackmore and Tsokri 2006, Li *et al*. 2006, Ding *et al*. 2013, Qiu *et al*. 2014, Sun *et al*. 2014, Natalini *et al*. 2013).

The proper orthogonal decomposition (POD) technique is a powerful method of data analysis aimed at obtaining low-dimensional approximate descriptions of the complex wind pressure field, thus can be used for compression of huge wind pressure data in support of aerodynamic database-aided structural design (Bienkiewicz *et al*. 1995, Davenport 1995, Holmes *et al*. 1997, Chen and Kareem 2005). The POD technique has also been used for modeling equivalent static wind load (ESWLs). Holmes (2002) suggested ESWL distribution as a linear combination of POD loading modes, where the combination factors depend on influence function of the response. A universal load distribution framework in terms of POD loading modes for a group of load effects were also suggested (e.g., Katsumura *et al*. 2007, Chen *et al*. 2014, Luo *et al*. 2017, Fiore *et al*. 2009, Chen and Yang *et al*. 2012). A new approach for modeling ESWLs based on the POD loading modes was proposed by Chen and Zhou (2007).

This paper examines the POD technique as applied to dynamic load and load effects of a low-rise cylindrical shell roof. The dynamic pressure statistics such as mean, standard deviation (STD), maximum and minimum, skewness and kurtosis are calculated from reduced-order representation with POD technique, and then compared with the results obtained from the original wind tunnel data. The effects of loading mode truncation on the predictions of various structural responses including node displacements, elements stresses and support reactions of the cylindrical shell roof are also addressed.

2. Wind tunnel experiments

Dynamic pressure measurements of a low-rise cylindrical shell roof model were conducted at an atmospheric boundary layer wind tunnel at Shantou University, China. The geometric scale ratio of the model is 1/60. The model has a length of 0.7 m, width of 0.5 m, edge height of 0.15 m, and arch height of 0.25 m as shown in Fig. 1. The rise span ratio is 0.2. The wind tunnel has a 3 m x 2 m cross-section and the atmospheric boundary layer for suburban terrain condition was simulated using the roughness elements and spires. 240 pressure taps were distributed at the surface of the rigid model as shown in Fig. 2. The dynamic wind pressure time series were measured simultaneously using vinyl tube of 70 cm long through a multi-channel pressure transducer system. The sampling frequency is 312.5 Hz, and a duration is 65.5 s. Fig. 3 shows the profiles of mean wind speed and longitudinal turbulence intensity. The power law exponent of mean wind

*Corresponding author, Professor
E-mail: xinzhong.chen@ttu.edu

ISSN: 1226-6116 (Print), 1598-6225 (Online)

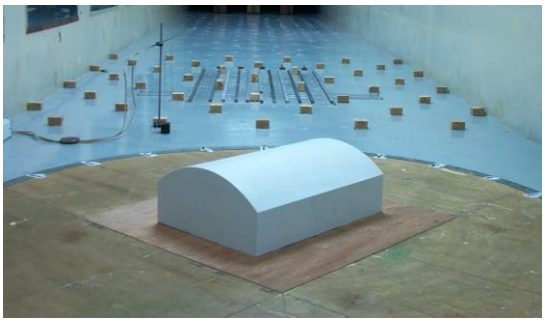

Fig. 1 Wind tunnel model of the structure

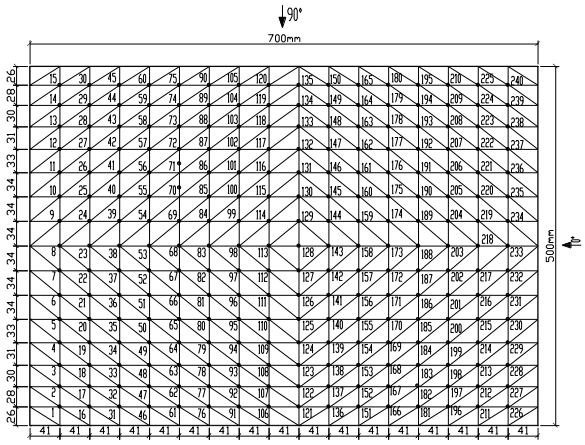

Fig. 2 Distribution of the pressure taps

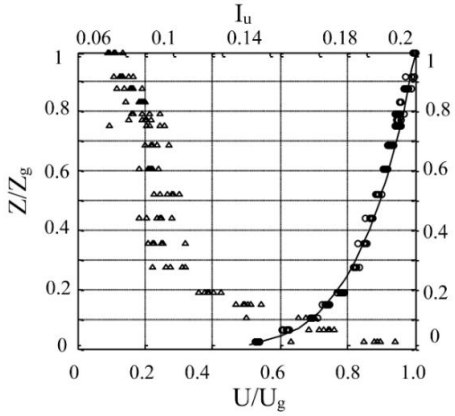

Fig. 3 Profiles of mean wind speed and turbulence intensity

speed profile is 0.15.

The wind speed U_g at the gradient height Z_g of 5.83 m is 17.58 m/s. Fig. 4 displays power spectral density (PSD) of the longitudinal turbulence at height of 0.6 m with the mean wind speed of 12.5 m/s. The turbulence intensity and integral length scale at 0.6 m are 0.18 and 0.43 m.

The design wind speed with a 50-year return period is 32.5 m/s at a height of 36 m in full scale (i.e., 26.8 m/s at 10 m height). Therefore, the wind speed scale in the wind tunnel test is 1/2.6. The time scale is 1/23, and the corresponding full scale time duration of pressure measurements is 25.1 minutes. The wind direction along with and normal to the longer side is defined as 0 and 90 degrees, respectively. In this study, the results of 90 degrees

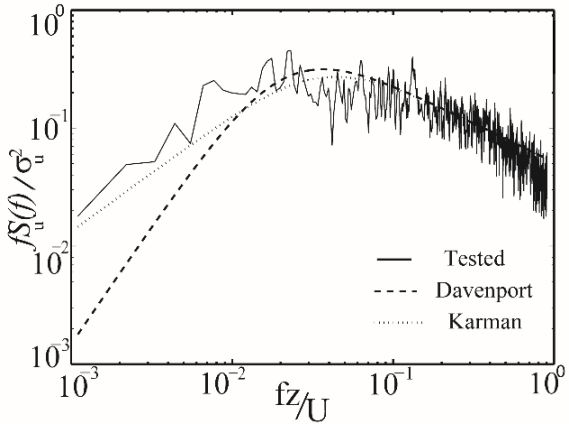

Fig. 4 PSD of longitudinal turbulence

are discussed.

The statistics of wind pressure coefficients such as mean, standard deviation (STD), maximum and minimum, skewness and kurtosis are shown in Fig. 5. The mean wind pressure is suction on surface of the roof. The pressure mean and STD on the top of roof are the biggest. The peak negative (minimum) pressure is also observed near the top of roof. The skewness and kurtosis are two important parameters for identifying pressure non-Gaussian properties. The kurtosis is bigger than 3 for pressures in the region near the support at leeward and windward, indicating softening non-Gaussian characteristics.

3. Reconstruction of wind pressure field based on POD

The original fluctuating wind pressure field $\{P(t)\}$ is expressed as (Chen and Kareem 2005)

$$\{P(t)\} = \sum_{n=1}^{N} \{\Phi\}_n a_n(t) \tag{1}$$

where $\{\Phi\}_n (n = 1,2,\cdots,N)$ are loading modes determined from the solution of the following eigenvalue problem:

$$[R_p]\{\Phi\}_n = \lambda_n \{\Phi\}_n \tag{2}$$

where $[R_p]$ is loading covariance matrix. The loading mode is normalized as $\{\Phi\}_n^T \{\Phi\}_n = 1$.

It can be readily proved that $\sum_{n=1}^{N} \sigma_{P_n}^2 = \sum_{n=1}^{N} \lambda_n$, i.e., the energy of the pressure field is identical to the sum of eigenvalues. The principle coordinates $a_n(t) (n = 1,2,\cdots,N)$ are calculated as follows by the orthogonal properties of eigenmodes:

$$a_n(t) = \{\Phi\}_n^T \{P(t)\} \tag{3}$$

By truncating the higher loading modes with lower eigenvalues, $\{P(t)\}$ is represented by a reduced-order model, thus data compression can be achieved:

$$\{P(t)\} \approx \sum_{n=1}^{M} \{\Phi\}_n a_n(t) \tag{4}$$

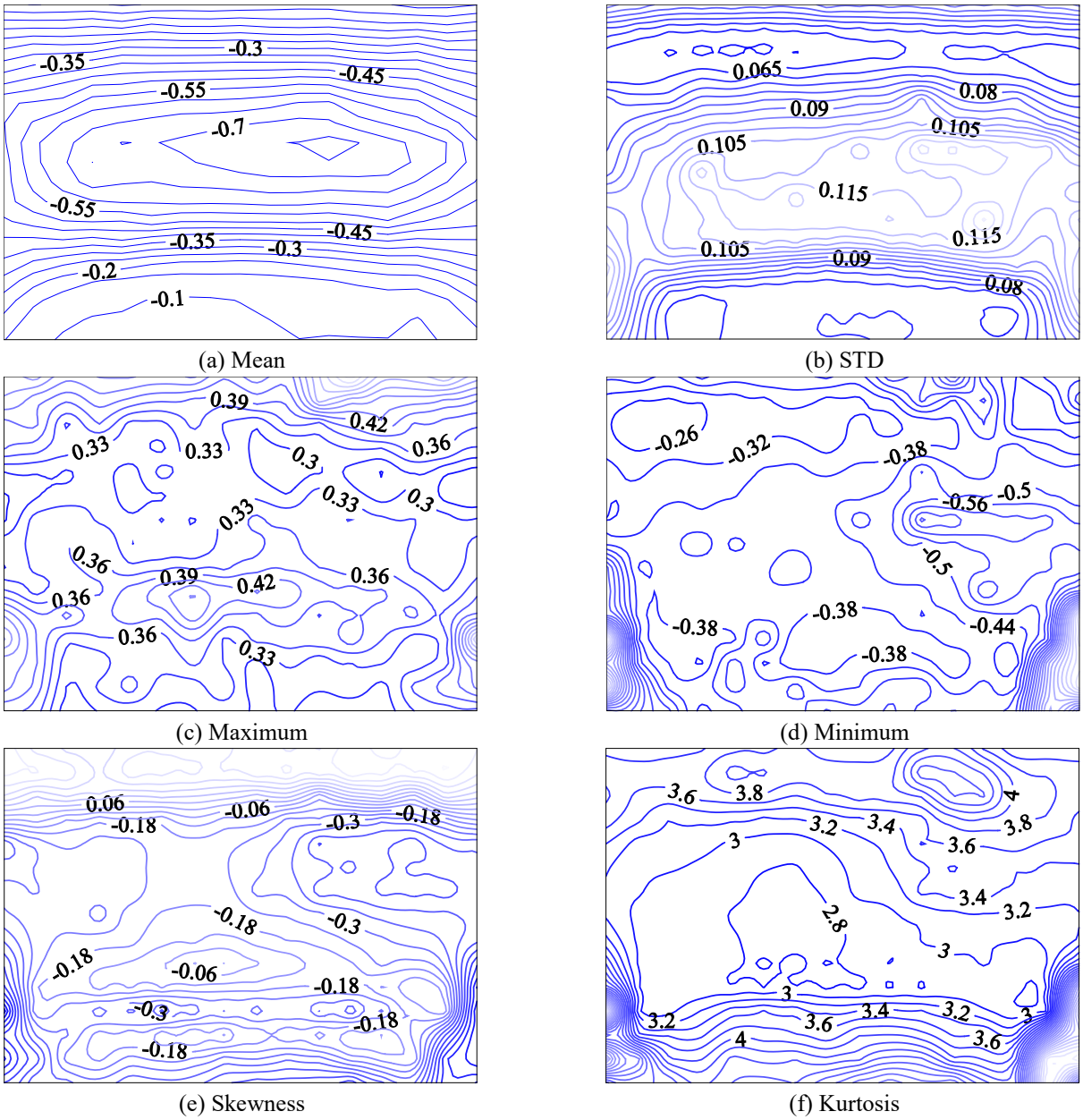

(a) Mean (b) STD

(c) Maximum (d) Minimum

(e) Skewness (f) Kurtosis

Fig. 5 Statistics of the wind pressure coefficients

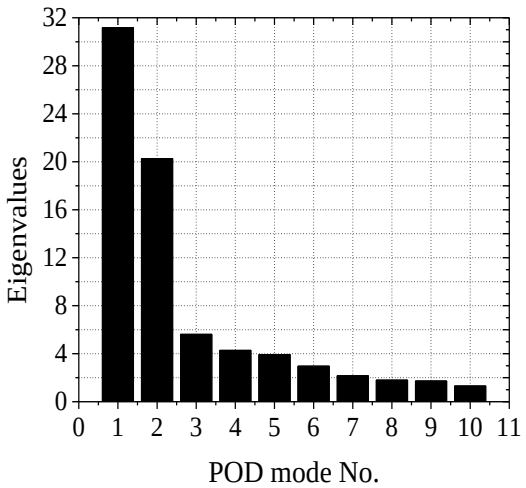

Fig. 6 POD eigenvalues of wind loads

where $M < N$.

Fig.6 shows the first ten higher eigenvalues of the loading covariance matrix. The first mode carries about 31% total energy, i.e., $\lambda_1/\sum\lambda_n$= 31%. The first two loading modes take 51% total energy. Fig.7 portrays the spatial distributions of first eight eigenvectors (loading mode shapes). The first and second loading modes are symmetric and asymmetric, respectively. The distribution characteristics of the loading modes provide useful connection with background response and modeling of equivalent static wind loads.

The dynamic pressure field is reconstructed with consideration of first 8, 80 and 130 loading modes. The STD, maximum and minimum are recalculated from the reconstructed pressures, and compared with the original values. The results are shown in Figs. 8, 9 and 10. It is

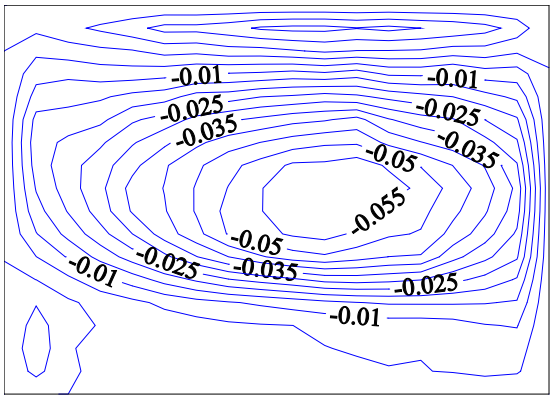

(a) 1st mode

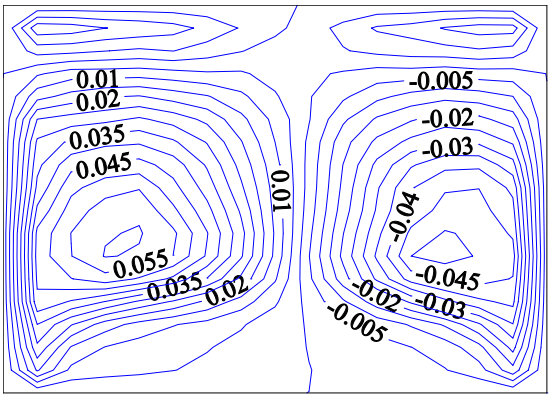

(b) 2nd mode

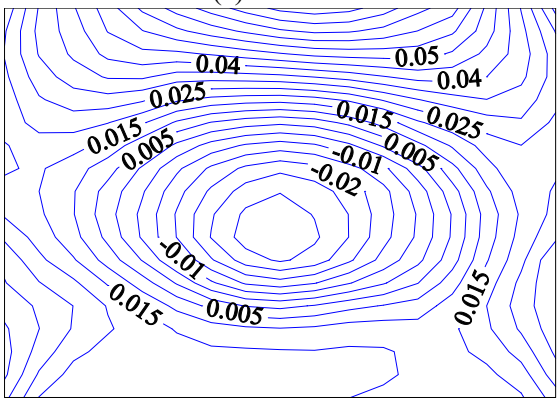

(c) 3rd mode

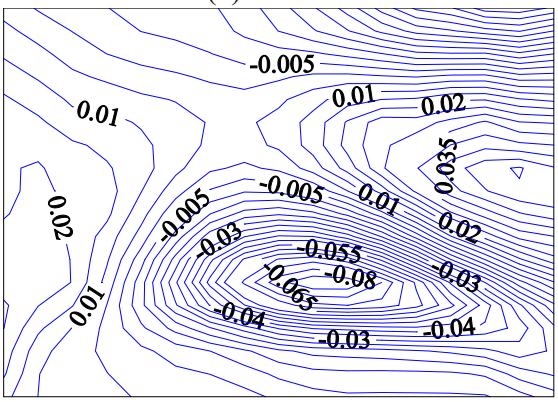

(d) 4th mode

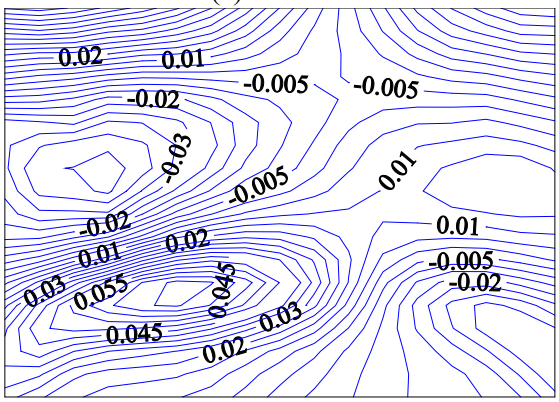

(e) 5th mode

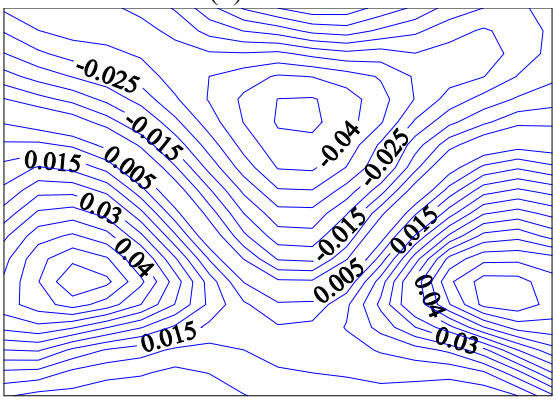

(f) 6th mode

Fig.7 First eight loading mode shapes

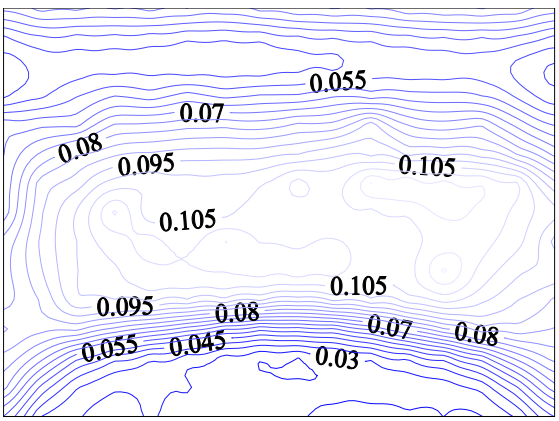

(a) 8 loading modes

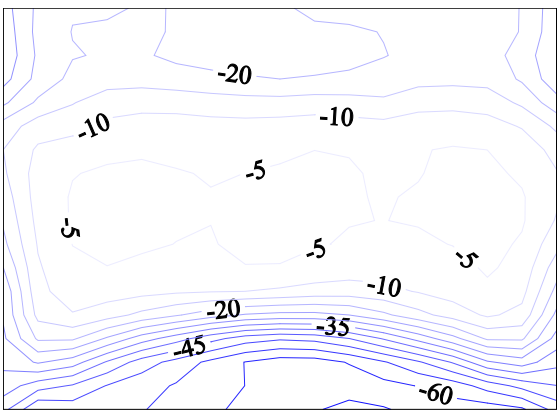

(b) Error of 8 loading modes

Fig. 8 Continued

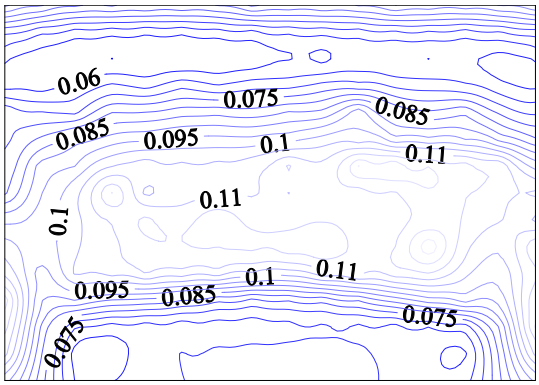

(c) 80 loading modes

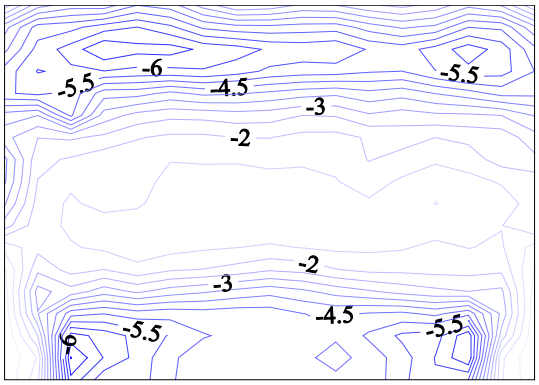

(d) Error of 80 loading modes

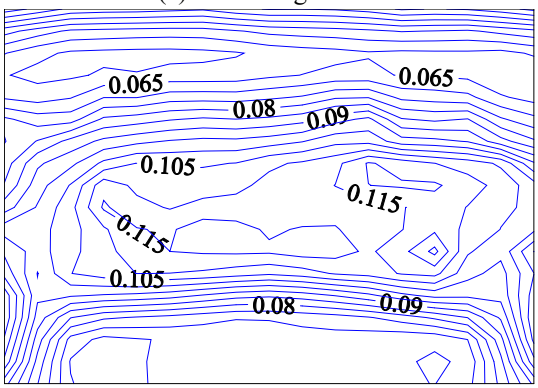

(e) 130 loading modes

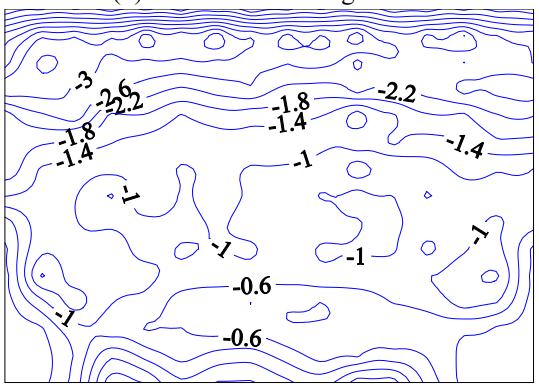

(f) Error of 130 loading modes

Fig. 8 STDs and errors of reconstructed pressure coefficients

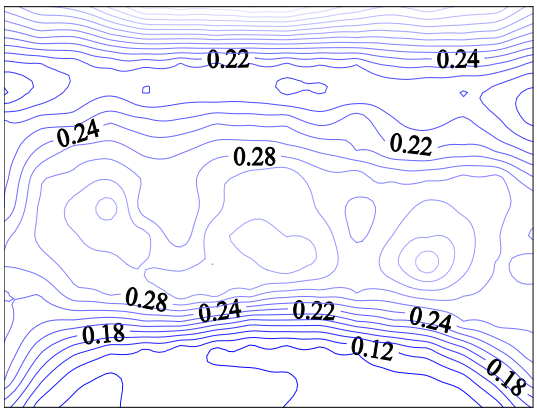

(a) 8 loading modes

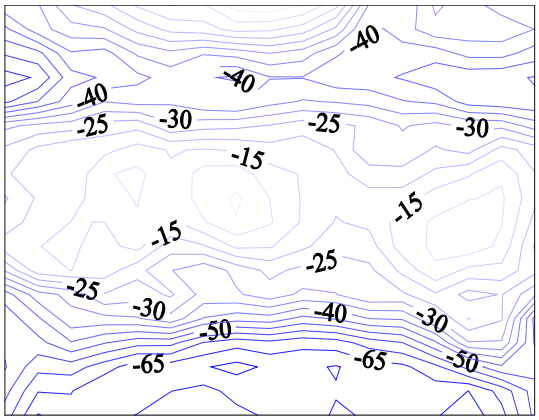

(b) Error of 8 loading modes

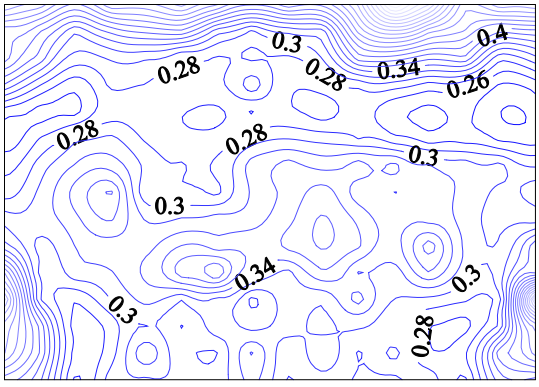

(c) 80 loading modes

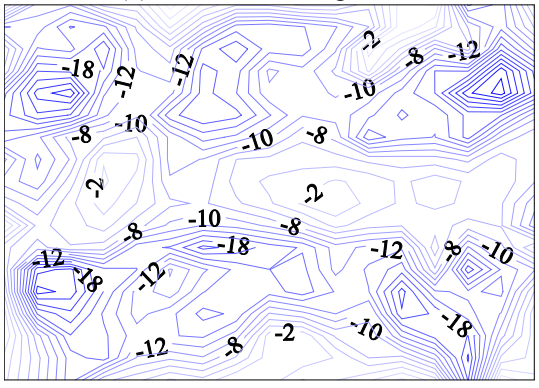

(d) Error of 80 loading modes

Fig. 9 Continued

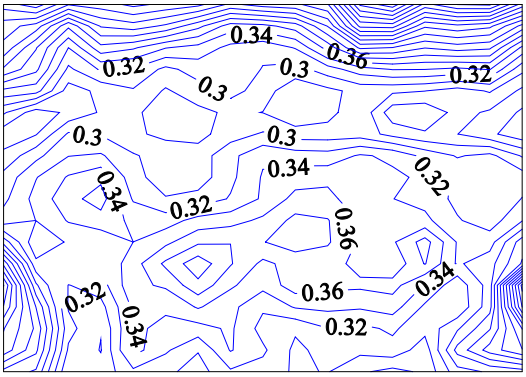

(e) 130 loading modes

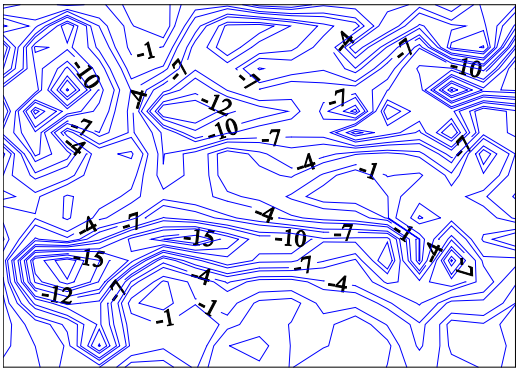

(f) Error of 130 loading modes

Fig. 9 Maximum values and errors of reconstructed pressure coefficients

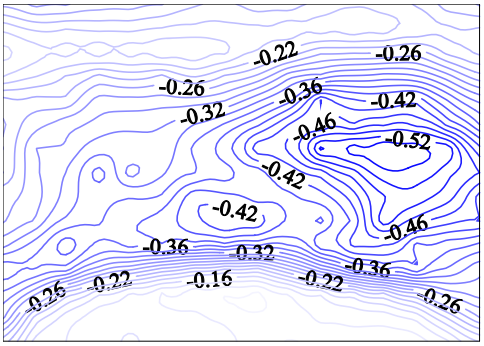

(a) 8 loading modes

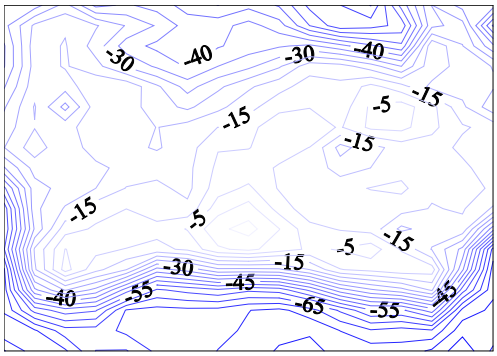

(b) Error of 8 loading modes

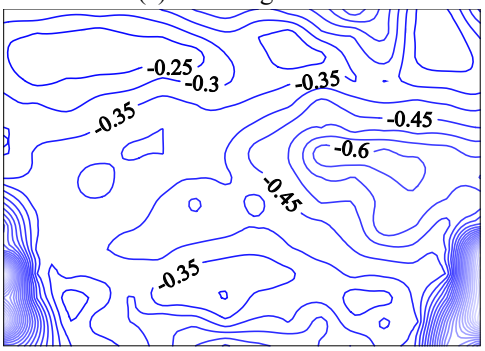

(c) 80 loading modes

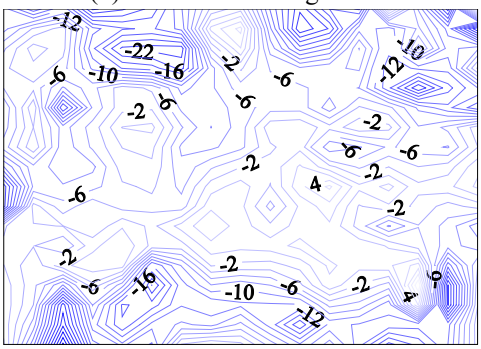

(d) Error of 80 loading modes

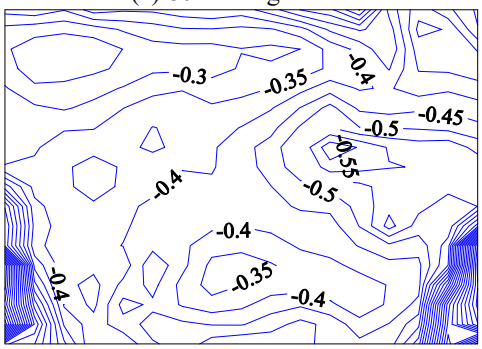

(e) 130 loading modes

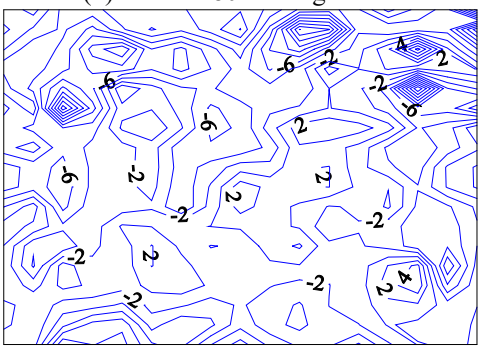

(f) Error of 130 loading modes

Fig. 10 Minimum values and errors of reconstructed pressure coefficients

observed that inclusion of 80 modes gives sufficiently accurate representation of STD. However, reproducing the maximum and minimum values need consideration of more loading modes. The reconstruction error for the maximum pressure near arc edge of the roof at windward is about 15% when 80 modes are included.

Fig. 11 shows original and reconstructed wind pressure series on pressure tap 162 (at the middle of the windward

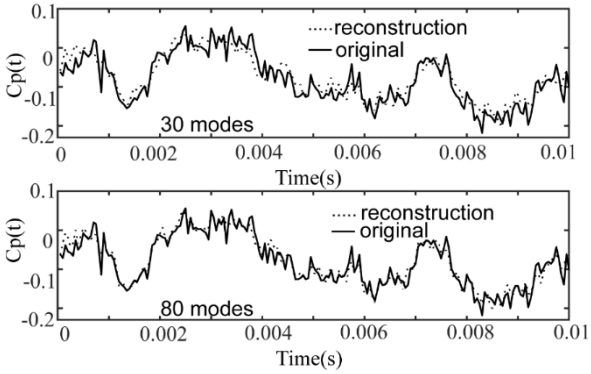

Fig. 11 Time history of the wind pressure coefficient (Tap 162)

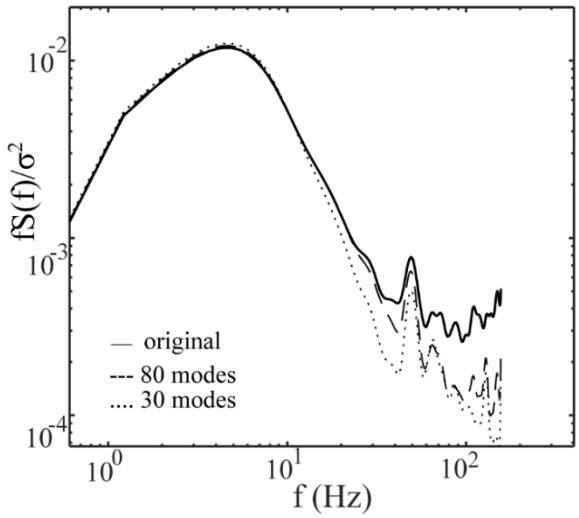

Fig. 12 Influence of POD mode truncation on the PSD of pressure coefficient (Tap 162)

Table 1 Statistics of the wind pressure coefficients influenced by the truncation of loading modes

Tap No.	Mode number	STD		Maximum		Minimum		Skewness		Kurtosis	
		Value	Error (%)	Value	Error (%)	Value	Error (%)	Value	Error (%)	Value	Error (%)
128	8	0.11	-2.7	0.31	-12.0	-0.39	-10.2	-0.29	27.4	2.86	-1.6
	15	0.11	-1.8	0.31	-10.9	-0.40	-7.9	-0.27	18.3	2.86	-1.5
	30	0.11	-2.1	0.32	-8.6	-0.43	-0.3	-0.27	17.4	2.89	-0.5
	80	0.11	-1.1	0.34	-2.9	-0.44	0.8	-0.23	3.3	2.91	-0.2
	All modes	0.11		0.35		-0.43		-0.23		2.90	
133	8	0.048	-23.8	0.20	-33.3	-0.20	-42.9	-0.15	-494.8	3.39	-13.1
	15	0.052	-17.5	0.24	-20.0	-0.24	-31.4	-0.08	-310.5	3.54	-9.2
	30	0.055	-12.7	0.25	-16.7	-0.25	-28.6	-0.09	-336.8	3.56	-8.7
	80	0.060	-4.8	0.28	-6.7	-0.32	-8.6	0.01	-88.8	3.78	-3.1
	All modes	0.063		0.30		-0.35		0.04		3.90	

side). Fig. 12 displays the comparison of their PSDs. It is evident that the truncation of higher loading modes causes errors only in higher-frequency range. The lower-frequency components of pressure field can be well represented by a small number of loading modes.

Table 1 summarizes the statistics of reconstructed wind pressure coefficients at Tap 128 (at the roof ridge) and 133 (at the middle of the windward side). It is observed that while first eight loading modes are sufficient for describing the total energy of the pressure field, an accurate representation of pressure statistics such as peak value (maximum or minimum) with an error less 5% requires more loading modes than that for STD.

4. Structural modal analysis

The cylindrical shell structure is a three-dimensional truss with steel pipe members. Two types of the cross sections are used: outer diameter of 60 mm and thickness of

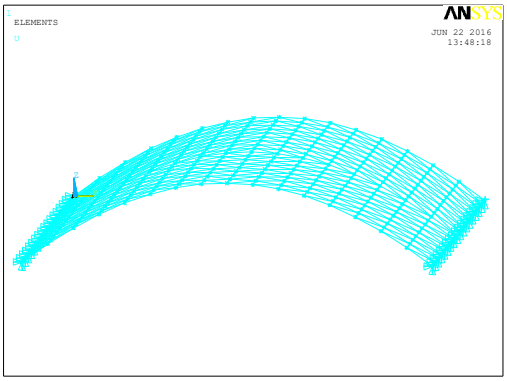

Fig. 13 FE model in ANSYS

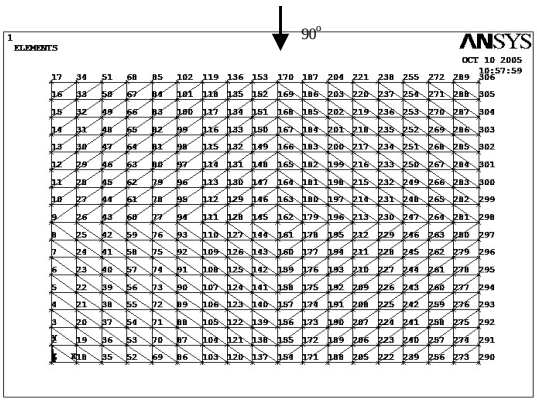

Fig. 14 Distribution of the nodes

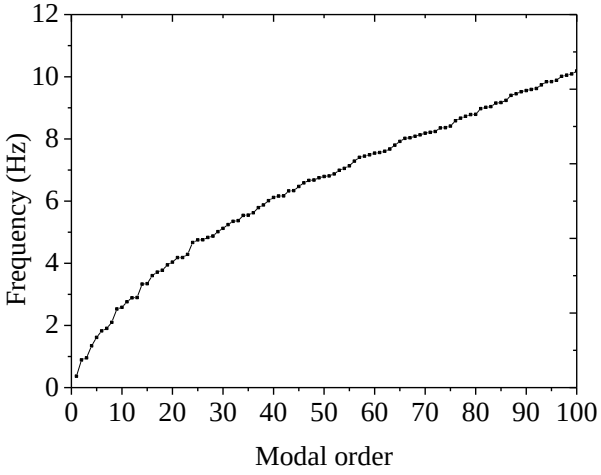

Fig. 15 First 100 modal frequencies

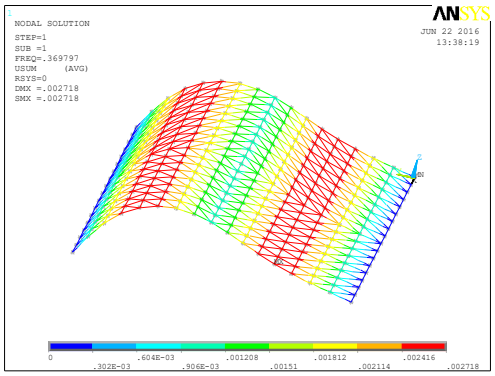

(a) First mode

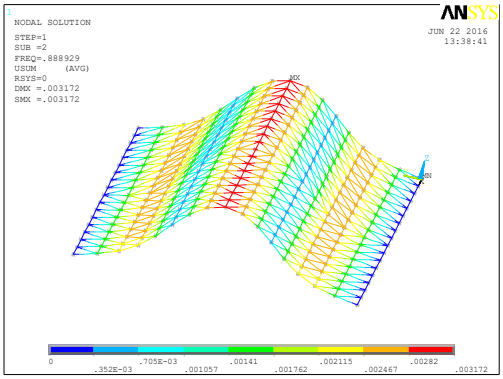

(b) Second mode

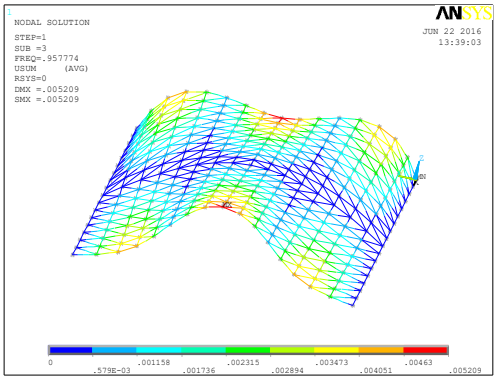

(c) Third mode

Fig. 16 Mode shapes of first three structural modes

3.5 mm; outer diameter of 159 mm and thickness of 5.0 mm. A finite element (FE) model of the structure was developed using the software ANSYS as shown in Fig. 13. The finite element analysis model has 306 nodes (Fig 14), 849 pipes elements and 36 support joints at both sides.

The modal frequencies are very close-spaced as shown in Fig. 15. The frequencies of the first one hundred modes are in the range from 0.37 Hz to 10.19 Hz. The shapes of the first three modes are shown in Fig. 16. The first mode shape represents the asymmetric horizontal vibration, while both the second and third mode shapes are associated with the vertical vibrations. The critical damping ratios for the first and second modes were set to be 2%, which were used to determine the Rayleigh damping matrix.

5. Prediction of background response

The fluctuating wind load effects of structures include background (quasi-static) and resonant components. The background wind load effects can be determined by a quasi-static analysis procedure. The background component of a response $r(t)$ of interest can be quantified as

$$r_B(t) = \sum_{j=1}^{N} \mu_j P_j(t) = \{\mu\}^T \{P(t)\} \quad (5)$$

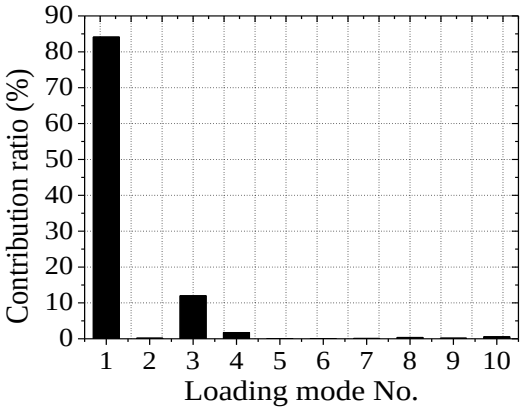

(a) z displacement at node 162

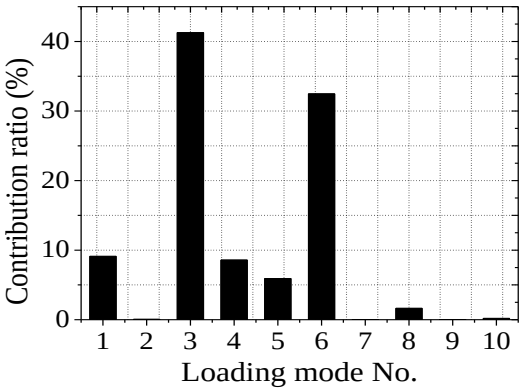

(b) z displacement at node 167

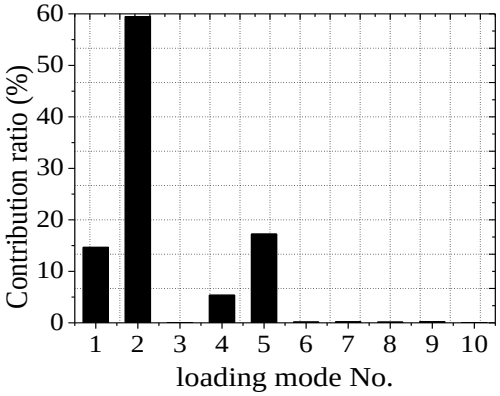

(c) x displacement at node 162

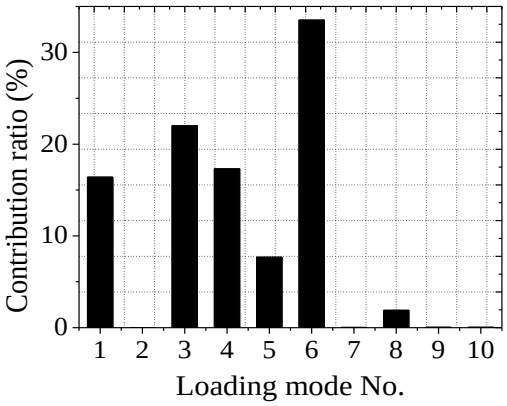

(d) y displacement at node 162

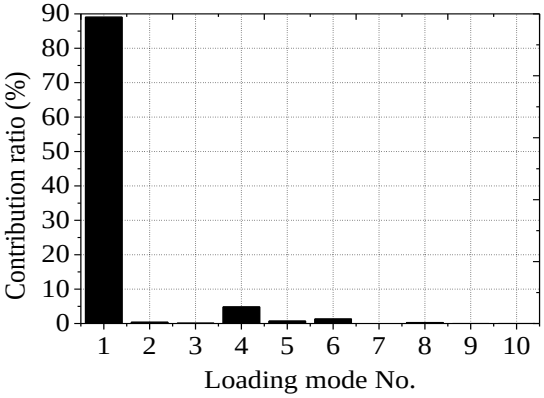

(e) Stress at element 775

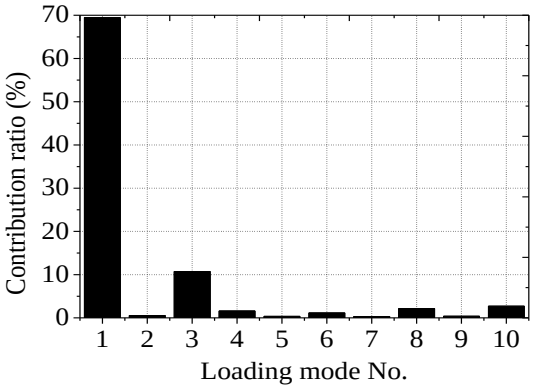

(f) Stress at element 793

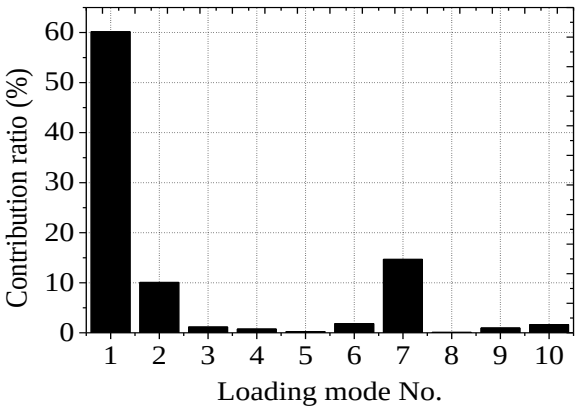

(g) Support reaction at node 51

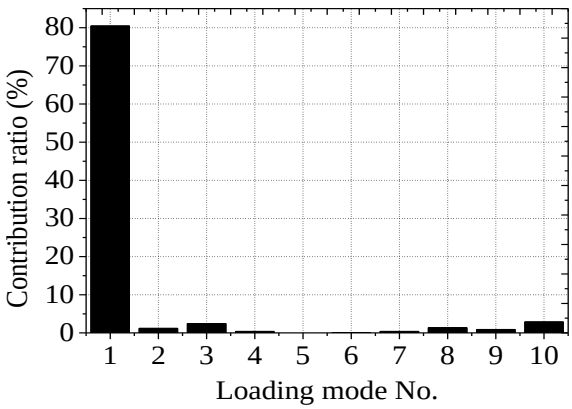

(h) Support reaction at node 153

Fig. 17 Contributions of loading modes to different background responses

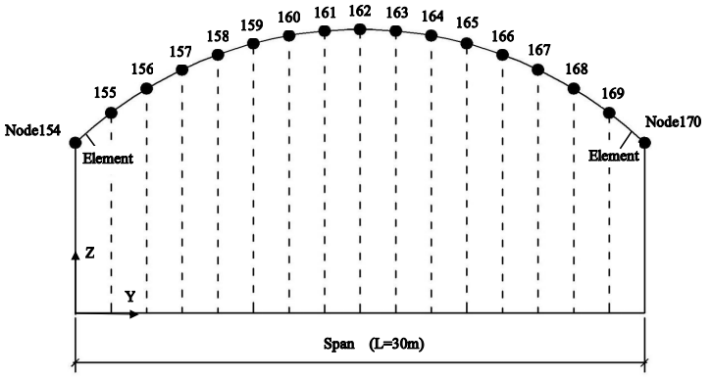

Fig. 18 Distribution of the typical nodes

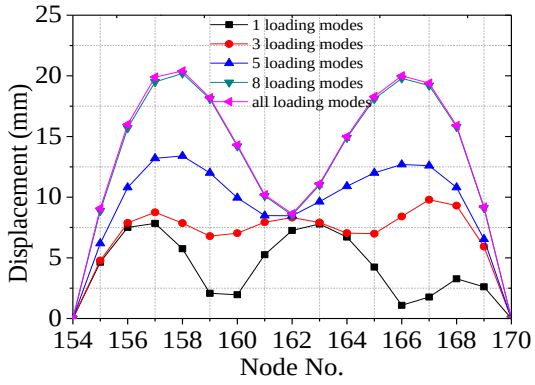

(a) Displacements in Z direction

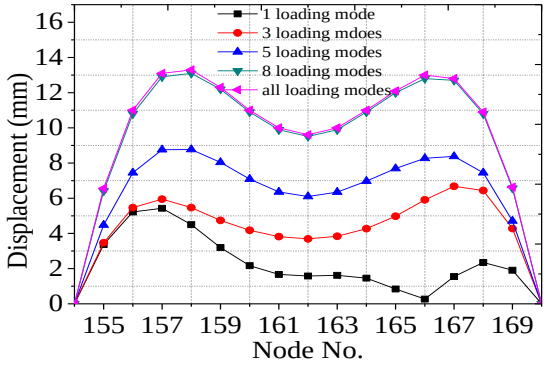

(b) Displacements in Y direction

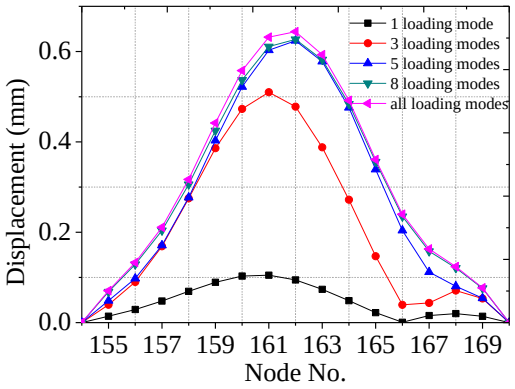

(c) Displacements in X direction

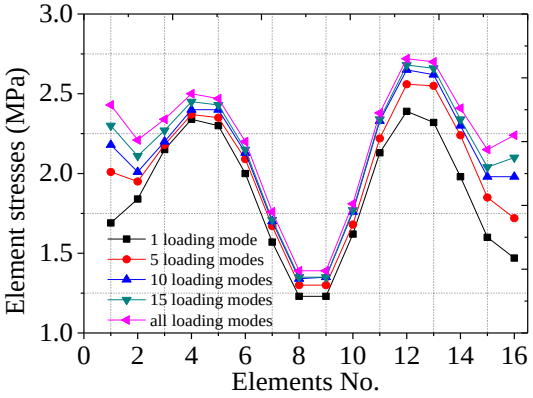

(d) Stresses

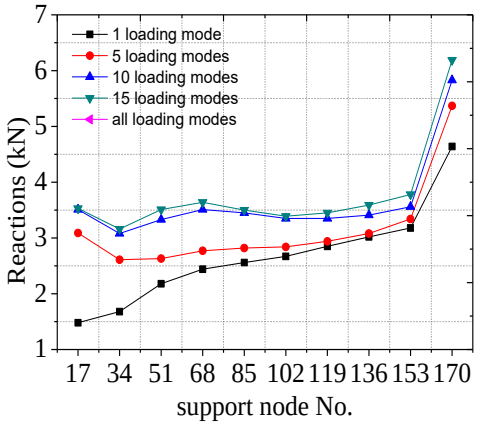

(e) Support reactions at one side

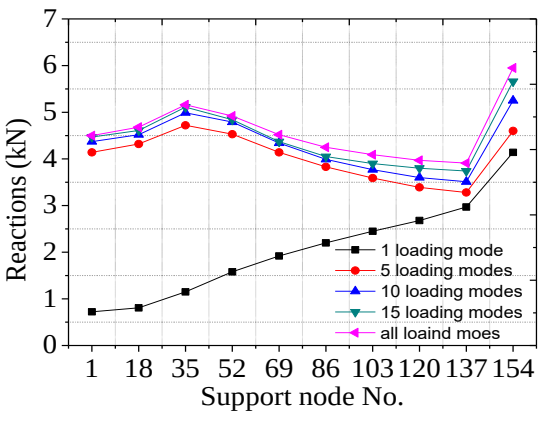

(f) Support reactions at another side

Fig. 19 Influence of loading modes on STDs of background responses

Table 2 Background response of the cylinder shell structure

	Elements stress (unit: MPa)				Reactions (unit: kN)			
No.	230	367	849	415	51	137	69	153
All modes	1.51	1.89	1.74	1.73	3.63	3.94	4.54	3.98
15 modes	1.48	1. 86	1.70	1.65	3.52	3.77	4.39	3.81
Error (%)	-2.21	-1.82	-2.35	-4.86	-3.11	-4.32	-3.41	-4.21
8 modes	1.38	1.80	1.71	1.62	3.23	3.34	4.34	3.44
Error (%)	-8.61	-4.69	-1.88	-6.38	-10.78	-15.28	-4.48	-13.58

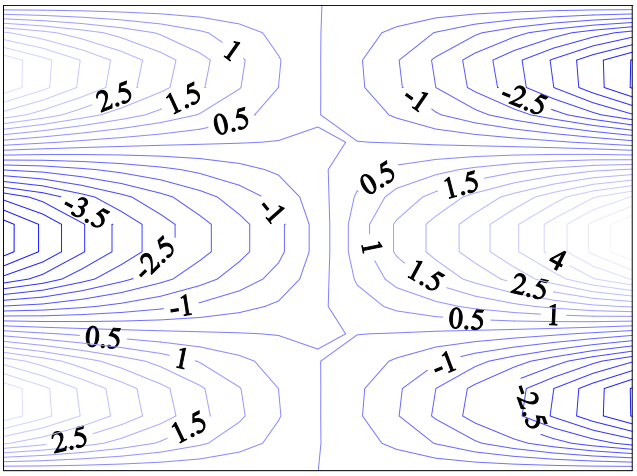

(a) X displacement at Node 162 (unit: mm/Nx10-5)

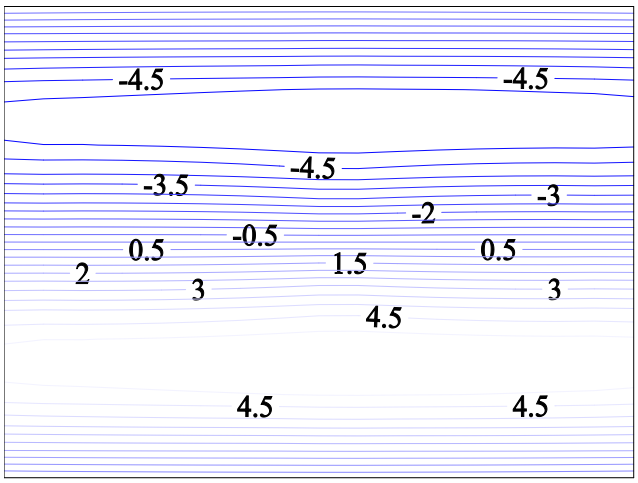

(b) Y displacement at Node 162 (unit: mm/Nx10^{-4})

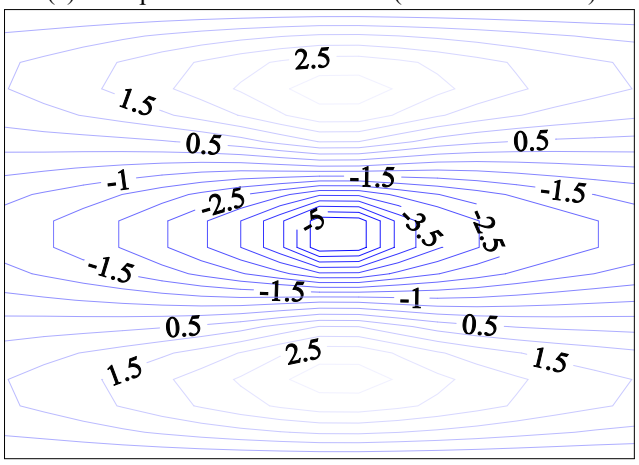

(c) Z displacement at Node 162 (unit: mm/Nx10-4)

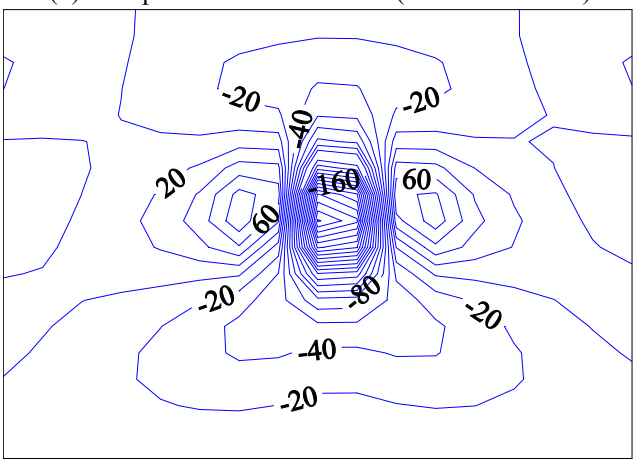

(d) Element stress at element 775 (unit: Pa/N)

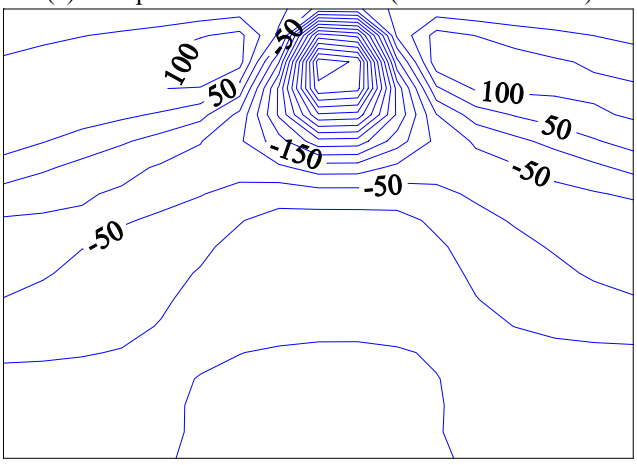

(e) Element stress at element 793(unit: Pa/N)

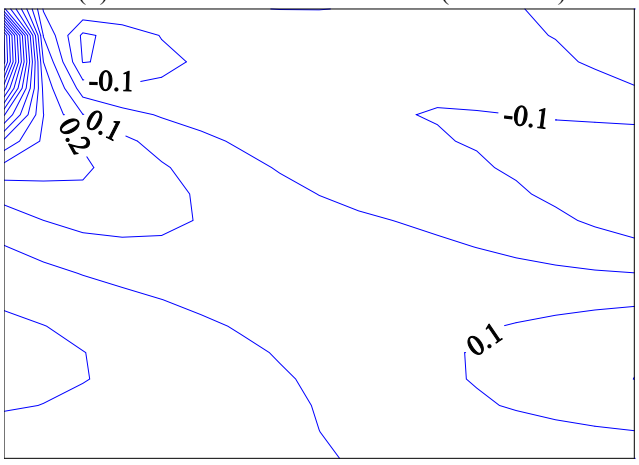

(f) Reaction at Node 51(unit: N/N)

Fig. 20 Influence coefficient surface of typical responses

where μ_j is influence coefficient indicating the static response value under unit load at *j*th location loading; $P_j(t)$ is wind load force at *j*th location.
The STD of background response is then determined as

$$\sigma_{r_B}^2 = \sum_{i,j} \mu_i \mu_j \rho_{ij} \sigma_{P_i} \sigma_{P_j} = \{\mu\}^T [R_p] \{\mu\} \quad (6)$$

where $\sigma_{P_i}$is STD of $P_j(t)$; ρ_{ij} is correlation coefficient between $P_i(t)$ and $P_j(t)$; $[R_p]$ is the $N \times N$ covariance matrix of the loading vector, which can be presented in terms of loading modes as

$$[R_p] = \sum_{n=1}^{N} \lambda_n \{\Phi\}_n \{\Phi\}_n^T \quad (7)$$

in which λ_n and $\{\Phi\}_n$ are *n*th eigenvalue and eigenvector, with the orthogonal property $\{\Phi\}_j^T \{\Phi\}_n = \delta_{jn}$ where δ_{jn} is the Kronecker delta. Accordingly (Chen and Zhou 2007)

$$\sigma_{r_B}^2 = \sum_{n=1}^{N} (r_n^{st})^2 \quad (8)$$

$$r_n^{st} = \{\mu\}^T \sqrt{\lambda_n} \{\Phi\}_n \quad (9)$$

It is observed that the STD of individual background response σ_{r_B} can be calculated as the combinations of response components associated with the POD loading modes using the square root of sum of square (SRSS) scheme. The response component r_n^{st} depends on the eigenvalue, spatial variation of loading mode shape and influence function. Clearly, the POD technique provides a useful linkage between the wind loading mode and the background response, and also for a convenient modeling of equivalent static load (Chen and Zhou 2007).

Fig. 17 shows the contributions of first 10 loading modes to the STD of background responses, including node displacements at node 162 and 167 (at the middle of the windward side), elements stresses at elements 775 and 793, and support reactions at node 51 (windward edge support point) and 153 (windward middle support point). It is observed that the displacement of node 162 in vertical z direction (x, y and z directions are defined in Fig. 18), stresses of elements 775 and 793, and two support reactions are dominated by the contribution of first loading mode. The third and six modes have dominant contributions to the displacement at node 167 in z direction. The displacement of node 162 in x direction is dominated by the second mode, while more mode contributions are observed in the displacement of node 162 in y direction. The effect of wind load modes to the element stresses and reaction forces are summarized in Table 2. The element stresses and support reactions require more loading modes be included for obtaining sufficiently accurate estimations than the displacements.

Fig. 18 displays the node numbers on centre ridge line of the roof. The STDs of background responses related to these nodes including displacements, stresses and support reactions are shown in Fig.19. It is observed that consideration of first 10 modes can lead to accurate estimation of the background responses.

The wind loading mode contribution to a specific response is determined by the similarity of loading mode shape and influence coefficient surface of the response (refer to Eq. (9)). Fig. 20 shows the influence coefficient surfaces of some interesting responses such as node displacement, support reactions and elements stresses. For example, the shape of the influence coefficient surface of the vertical displacement response at node 162 is symmetric, thus the first loading mode which has asymmetric mode shape contributes less to this response.

6. Dynamic response including both background and resonant components

Based on random vibration theory, the dynamic response $r(t)$ is given by modal displacement vector $q(t)$ and the PSD of $r(t)$ is estimated as

$$r(t) = \{G\}^T \{q(t)\} \quad (10)$$

$$[S_q(f)] = [H(f)][\Psi]^T [S_p(f)][\Psi][H(f)]^* \quad (11)$$

$$S_r(f) = \{G\}^T [S_q(f)] \{G\} \quad (12)$$

where $[H(f)]$ is transfer matrix of the modal displacements; $\{G\} = \{\mu\}[M][\Psi][\Lambda]$ is modal participation coefficient; $\{\mu\}$ is influence matrix defined as the response under a unit load; $[\Psi]$ is structural mode shape matrix; $[M]$ is mass matrix in physical coordinates; $[\Lambda]$ = diag$[\omega_j^2]$; $\omega_j$is *j*th structural modal frequency.

The background and resonant response components are quantified through the integration of response spectrum at different frequency ranges. The separation frequency between background and resonant response is $0.5f_1$ (f_1 is first structural frequency). Table 3 shows the contributions of structural modal responses to background and resonant responses in terms of node displacements, element stresses and horizontal support reactions. Calculation of background displacement needs contributions of 10 modes, while the resonant response only needs 3 modes. The calculation of background and resonant components of support reactions requires consideration of 80 modes. The resonant component of the element stress needs 50 modes. It is more efficient to compute the background response based on POD loading modes as previously discussed. The ratio between the resonant and background components depends on the external wind load and dynamic characteristics of the cylindrical shell structure. The resonant response component is significant for elements stresses. Fig. 21 shows contributions of structural modes to some responses at typical nodes and elements. The background displacement at nodes 162 and 167 may be obtained only with first ten structural modes. The background reactions F_y, i.e., horizontal support reaction at nodes 51 and 137 (Fig. 21(c) and Fig. 21(d)) need consideration of higher structural modes. Some higher structural modes have significant contribution to background and resonant responses, such as 51th mode for response at element 469.

Table 4 show the correlation coefficients between first 5

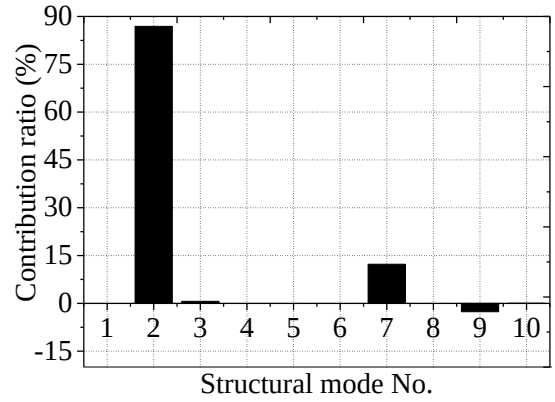

(a) Background displacement at node 162

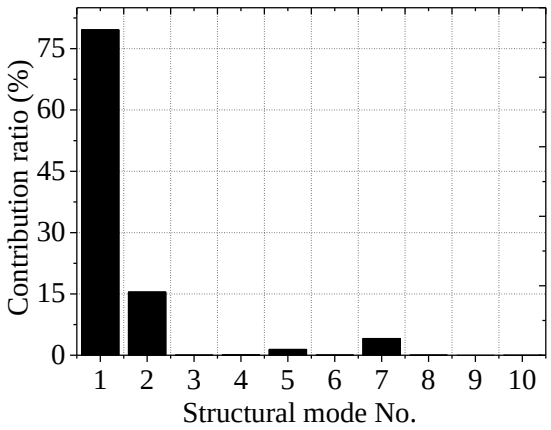

(b) Background displacement at node 167

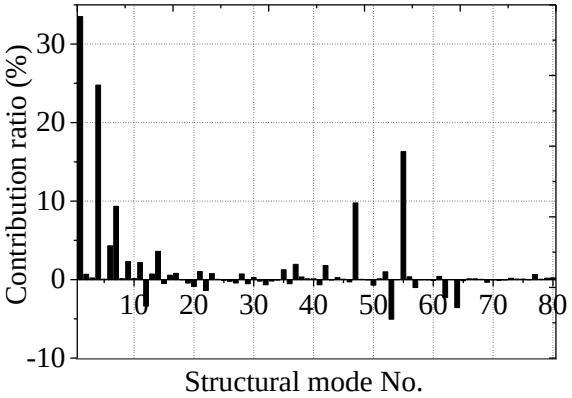

(c) Background reaction F_y at node 51

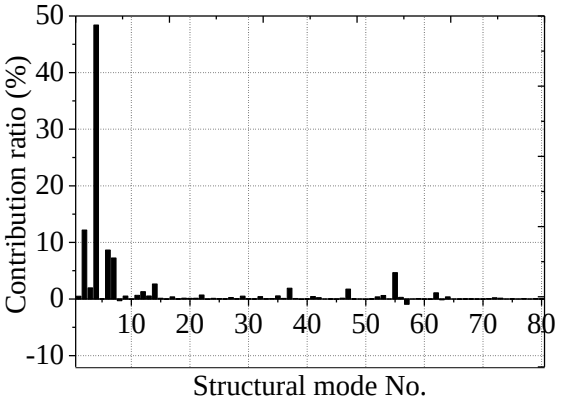

(d) Background reaction F_y at node 137

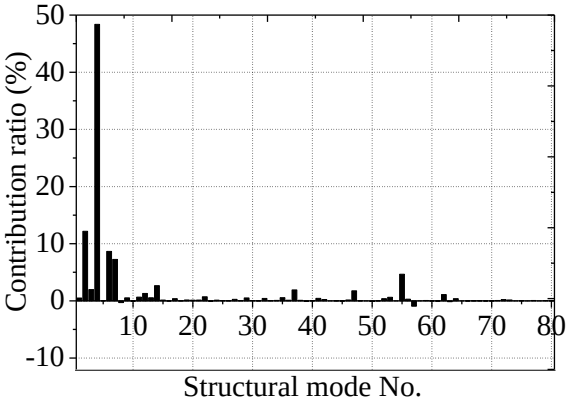

(e) Resonant reaction F_y at node 51

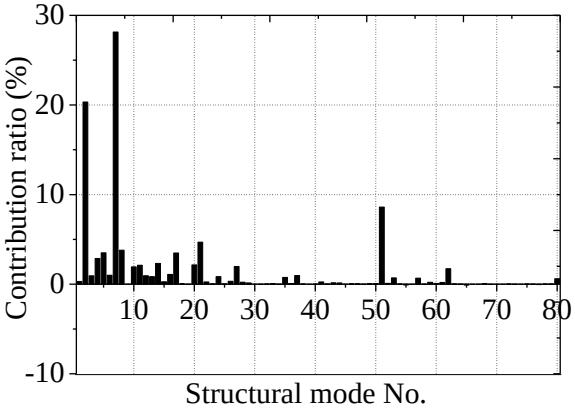

(f) Resonant reaction F_y at node 137

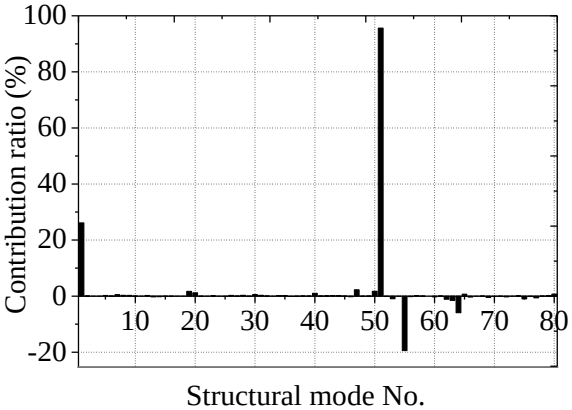

(g) Background stress at element 469

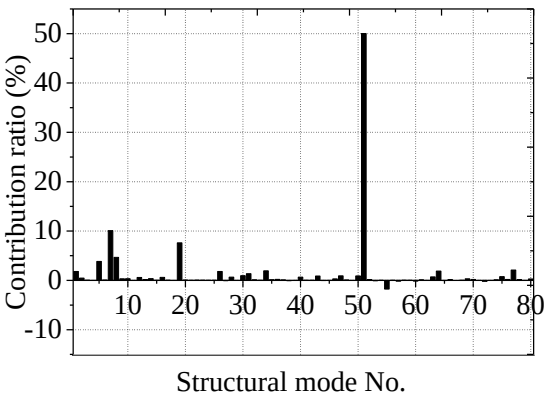

(h) Resonant stress at element 469

Fig. 21 Contribution of structural modes to responses

Table 3 Background and Resonant components of responses

(a) Displacement				
		Displacement (mm)		
	No.	158	162	167
Background	Original	8.67	8.51	9.74
	5 modes	8.72	7.44	9.41
	Error (%)	0.58	-12.57	-3.39
	10 modes	8.78	8.27	9.82
	Error (%)	1.27	-2.82	0.82
Resonant	Original	2.30	8.11	2.22
	3 modes	2.30	8.01	2.22
	Error (%)	-0.03	-1.30	-0.03
	5 modes	2.30	8.01	2.22
	Error (%)	-0.01	-1.30	-0.01
	Ratio (R/B)	0.27	0.95	0.23

Table 3 Background and Resonant components of responses

(b) Element stress and reactions									
		Element stress (MPa)				Reaction force (kN)			
	No.	230	367	849	415	51	69	137	153
Background	Original	1.53	1.97	1.90	1.80	3.79	4.72	4.02	4.13
	50 modes	1.51	1.92	1.82	1.91	3.44	3.19	1.99	2.24
	Error (%)	-1.31	-2.54	-4.21	6.11	-9.23	-32.41	-50.50	-45.76
	80 modes	1.53	1.95	1.96	1.80	3.71	4.54	3.99	4.11
	Error (%)	-1.01	-1.01	3.16	-0.20	-2.11	-3.81	-0.75	-0.48
Resonant	Original	2.04	2.28	2.43	2.80	3.84	3.86	4.01	3.84
	50 modes	2.03	2.27	2.40	2.79	3.57	3.51	3.50	3.34
	Error (%)	-0.49	-0.44	-1.23	-0.36	-7.03	-9.06	-12.72	-13.02
	80 modes	2.04	2.28	2.44	2.80	3.84	3.86	4.01	3.84
	Error (%)	-0.11	-0.11	-0.10	-0.11	-0.11	-0.10	-0.10	-0.11
	Ratio(R/B)	1.33	1.16	1.29	1.56	1.01	0.82	1.00	0.93

Table 4 Correlation coefficients between modal response components of reaction Fy at node 51

Mode order	1	2	3	4	5
1	1.00	-0.17	-0.04	-0.00	0.09
2		1.00	0.03	0.02	0.05
3			1.00	0.11	0.00
4	Symmetric			1.00	-0.01
5					1.00

modal response components of reaction F_y at node 51. The modal correlation coefficients are quit small. This indicates that the modal responses can be combined using square-root-of-square (SRSS) method for the total response.

7. Conclusions

The effectiveness of POD technique was examined as applied to wind load and load effects of a cylindrical shell roof. The reconstruction of dynamic wind pressures with reduced-order modeling through POD technique required 80 loading modes for accurate representation of STDs of pressures, while more modes were needed for the extreme pressures. Truncation of higher modes led to the loss of higher frequency components of pressures. The estimation of background node displacements required consideration of 6 loading modes, while 15 modes were needed for background support reactions and element stresses. Larger number of structural modes were needed for these background responses when calculated by structural modal analysis. For instance, 80 structural modes were needed for the background support reactions. The calculation of background response by using POD loading modes was more effective and physically meaningful.

Acknowledgment

The support this work was provided in part by the NNSF Grant No.50908077. This support is gratefully acknowledged.

References

Bienkiewicz B., Tamura Y., Ham H., Ueda H. and Hibi K. (1995), "Proper orthogonal decomposition and reconstruction of multi-channel roof pressure", *J. Wind. Eng. Ind. Aerod.*, **54**, 369-381.

Blackmore P. and Tsokri E. (2006), "Wind load on curved roofs", *J. Wind. Eng. Ind. Aerodyn.*, **94**(11), 833-844.

Chen X. and Kareem A. (2005), "Proper orthogonal decomposition-based modeling, analysis, and simulation of dynamic wind load effects on structures", *J. Eng. Mech.*, **131**(4),

325-339. https://doi.org/10.1061/(ASCE)0733-9399(2005)131:4(325).

Chen X. and Zhou N. (2007), "Equivalent static wind loads on low-rise buildings based on full-scale pressure measurements", *Eng. Struct.*, **29**(10), 2563-2575. https://doi.org/10.1016/j.engstruct.2007.01.007.

Chen B., Yan X. and Yang Q. (2014), "Wind-induced response and universal equivalent static wind loads of single layer reticular dome shells", *Int. J. Struct. Stabil. Dyn.*, **14**(4), 1450008. https://doi.org/10.1142/S0219455414500084.

Chen B., Yang Q. and Wu Y. (2012), "Wind-induced response and equivalent static wind loads of long span roofs", *Adv. Struct. Eng.*, **15**(7), 1099-1114. https://doi.org/10.1142/S0219455414500084.

Ding Z. and Tamura Y. (2013), "Contributions on wind-induced overall and local behaviors for internal forces in cladding support components of large-span roof structure", *J. Wind. Eng. Ind. Aerod*., **115**, 162-172. https://doi.org/10.1016/j.jweia.2013.01.013.

Davenport A.G. (1995), "How can we simplify and generalize wind loads", *J. Wind. Eng. Ind. Aerod*., **54**, 657-669. https://doi.org/10.1016/0167-6105(94)00079-S.

Franchini S., Pindado S., Meseguer J. and Sanz-Andrés A. (2005), "A parametric, experimental analysis of conical vortices on curved roofs of low-rise buildings", *J. Wind. Eng. Ind. Aerod*., **93**(8), 639-650. https://doi.org/10.1016/j.jweia.2005.07.001.

Fiore A. and Monaco, P. (2009), "POD-based representation of the along wind equivalent static force for long-span bridges", *Wind Struct.*, **12**(3), 239-257.

Holmes, J.D., Sankaran, R., Kwok, K.C.S and Syme, M.J. (1997), "Eigenvector modes of fluctuating pressures on low-rise building modes", *J. Wind. Eng. Ind. Aerod*., **69**, 697-707.

Holmes, J.D. (2002), "Effective static load distributions in wind engineering", *J. Wind. Eng. Ind. Aerod*., **90**(2), 91-109. https://doi.org/10.1016/S0167-6105(01)00164-7.

Katsumura, A., Tamura Y. and Nakamura, O. (2007), "Universal wind load distribution simultaneously reproducing largest load effects in all subject members on large-span cantilevered roof", *J. Wind. Eng. Ind. Aerodyn*., **95**(9-11), 1145-1165.

Li, Y., Tamura, Y., Yoshida, A., Katsumura, A. and Cho, K. (2006), "Wind loading and its effects on single-layer reticulated cylindrical shells", *J. Wind. Eng. Ind. Aerod*., **94**(12), 949-973. https://doi.org/10.1016/j.jweia.2006.04.004.

Luo, N., Liao, H. and Li, M. (2017), "An efficient method for universal equivalent static wind loads on long-span roof structures", *Wind and Struct.*, **25**(5), 493-506. https://doi.org/10.12989/was.2017.25.5.493.

Natalini, M., Morel, C. and Natalini, B. (2013), "Mean load on vaulted canopy roofs", *J. Wind. Eng. Ind. Aerod*., **119**, 102-113. https://doi.org/10.1016/j.jweia.2013.05.001.

Qiu, Y., Sun, Y., Wu, Y. and Tamura, Y. (2014), "Modeling the mean wind loads on cylindrical roofs with consideration of the Reynolds number effect in uniform flow with low turbulence", *J. Wind. Eng. Ind. Aerod*., **129**, 11-21. https://doi.org/10.1016/j.jweia.2014.02.011.

Sun, Y., Wu, Y., Qiu, Y. and Tamura, Y. (2014), "Effects of free-stream turbulence and Reynolds number on the aerodynamic characteristics of a semi cylindrical roof", *J. Struct. Eng.*, **141**(9), 04014230. https://doi.org/10.1061/(ASCE)ST.1943-541X.0001209.